A&A 662, A113 (2022)
https://doi.org/10.1051/0004-6361/202243618
© A. Sahade et al. 2022

Astronomy & Astrophysics

# Pseudostreamer influence on flux rope evolution*

A. Sahade[1,2,3], M. Cécere[1,3], M. V. Sieyra[4], G. Krause[5,6], H. Cremades[7], and A. Costa[1]

[1] Instituto de Astronomía Teórica y Experimental, CONICET-UNC, Córdoba, Argentina
e-mail: mariana.cecere@unc.edu.ar
[2] Facultad de Matemática, Astronomía, Física y Computación, Universidad Nacional de Córdoba (UNC), Córdoba, Argentina
[3] Observatorio Astronómico de Córdoba, UNC, Córdoba, Argentina
[4] Centre for mathematical Plasma Astrophysics, Department of Mathematics, KU Leuven, Celestijnenlaan 200B, 3001 Leuven, Belgium
[5] Instituto de Estudios Avanzados en Ingeniería y Tecnología, CONICET, Córdoba, Argentina
[6] Facultad de Ciencias Exactas, Físicas y Naturales, UNC, Córdoba, Argentina
[7] Grupo de Estudios en Heliofísica de Mendoza, CONICET, Universidad de Mendoza, Mendoza, Argentina

Received 23 March 2022 / Accepted 16 May 2022

**ABSTRACT**

*Context.* A highly important aspect of solar activity is the coupling between eruptions and the surrounding coronal magnetic field topology, which determines the trajectory and morphology of the ejected plasma. Pseudostreamers (PSs) are coronal magnetic structures formed by arcs of twin loops capped by magnetic field lines from coronal holes of the same polarity that meet at a central spine. PSs contain a single magnetic null point in the spine, immediately above the closed field lines, which potentially influences the evolution of nearby flux ropes (FRs).

*Aims.* Because of the impact of magnetic FR eruptions on space weather, we aim to improve current understanding of the deflection of coronal mass ejections (CMEs). To understand the net effect of PSs on FR eruptions, it is first necessary to study diverse and isolated FR–PS scenarios that are not influenced by other magnetic structures.

*Methods.* We performed numerical simulations in which a FR structure is in the vicinity of a PS magnetic configuration. The combined magnetic field of the PS and the FR results in the formation of two magnetic null points. We evolve this scenario by numerically solving the magnetohydrodynamic equations in 2.5D. The simulations consider a fully ionised compressible ideal plasma in the presence of a gravitational field and a stratified atmosphere.

*Results.* We find that the dynamic behaviour of the FR can be categorised into three different classes based on the FR trajectories and whether it is eruptive or confined. Our analysis indicates that the magnetic null points are decisive in the direction and intensity of the FR deflection and their hierarchy depends on the topological arrangement of the scenario. Moreover, the PS lobe acts as a magnetic cage enclosing the FR. We report that the total unsigned magnetic flux of the cage is a key parameter defining whether or not the FR is ejected.

**Key words.** Sun: coronal mass ejections (CMEs) – magnetohydrodynamics (MHD) – methods: numerical

## 1. Introduction

Magnetic flux ropes (FRs) are thought to be the central structures of solar eruptions, including prominence and filament eruptions, flares, and coronal mass ejections (CMEs). The physical process connecting these phenomena is the eruption of the magnetic FR system (Zhang et al. 2001; van Driel-Gesztelyi & Green 2015; Green et al. 2018; Jiang et al. 2018; Yang et al. 2018; Filippov 2019). Knowing whether or not the FR will erupt is naturally fundamental to predicting a CME event. Gronkiewicz et al. (2016) pointed out several mechanisms that can decelerate and confine eruptions in the corona. The first is the action of gravity, which prevents the eruption when the energy of the FR is not enough to escape the gravitational potential of the Sun (Filippov 2021). Even if the FR has the energy to escape gravity, the eruption will be confined if the overlying arcade field – whose lines form a magnetic cage – is too strong or does not quickly decay with height (Török & Kliem 2005; Wang & Zhang 2007; Chen et al. 2013; Amari et al. 2018; Baumgartner et al. 2018; Jing et al. 2018). Recently, Li et al. (2020, 2021, 2022) proved that there exists a negative correlation between flare eruptivity (i.e., if it has an associated CME) and the total unsigned magnetic flux of the active region producing the flare, which describes the strength of the background field confinement.

Once the eruption occurs, it is essential to understand the path that a CME will follow in order to predict its geoeffectiveness. This requires knowledge of any non-radial propagation of the CME, for which deflections in the trajectory must be studied. It is widely known that the magnetic structures in the vicinity of FRs are capable of deflecting them both in latitude and longitude. While coronal holes (CHs; e.g., Cremades et al. 2006; Gopalswamy et al. 2009; Sahade et al. 2020, 2021) and active regions (e.g., Kay et al. 2015; Möstl et al. 2015; Wang et al. 2015) deflect FRs away from their location, heliospheric current sheets (e.g., Liewer et al. 2015; Wang et al. 2020), helmet-streamers (e.g., Zuccarello et al. 2012; Yang et al. 2018), and pseudostreamers (PSs; e.g., Bi et al. 2013; Wang 2015; Cécere et al. 2020; Wang et al. 2020) attract FRs towards their low magnetic energy regions. The combined effect of the several structures at different heights was shown by, for example, Sieyra et al. (2020). In previous studies (Sahade et al. 2020,

* Movie associated with Fig. 5 is available at https://www.aanda.org



Open Access article, published by EDP Sciences, under the terms of the Creative Commons Attribution License (https://creativecommons.org/licenses/by/4.0), which permits unrestricted use, distribution, and reproduction in any medium, provided the original work is properly cited.
This article is published in open access under the Subscribe-to-Open model. Subscribe to A&A to support open access publication.

2021), we found that the presence of a coronal hole near to the eruptive region forms a magnetic null point that attracts the FR. The null point can be located between the FR and CH (in the case of anti-aligned polarities) or at the other side of the FR (aligned polarities). The first scenario produces an initial deflection towards the CH and a second deflection away from its position, but the second leads to a single deflection in which the FR moves away from the CH. All the final paths lead away from the location of the coronal hole by the 'channelling' of the magnetic field lines, that is, the FR is guided to follow the path of least resistance. Möstl et al. (2015) and Wang et al. (2015) studied an event on 2014 January 7 whose deflection seems to be caused by the magnetic pressure gradient from a nearby active region and whose final path is also channelled by the configuration of the magnetic field lines in the direction of least resistance. Shen et al. (2011) concluded that the trajectory in the early stages is influenced by the background magnetic energy gradients, causing the CME to propagate towards the region with the lowest magnetic energy density. Similar results were found by Sieyra et al. (2020) where most of the analysed CMEs were aligned in the direction of the magnetic energy decrease. These latter authors also showed that most of the deflection occurs at heights of lower than $2.4\,R_{\odot}$, suggesting that it is of utmost importance to study the trajectory in the early stages of eruptions.

Streamers are characterised by containing a region of null magnetic energy, and therefore they can act as a potential well attracting CMEs towards them (Kay et al. 2013). In particular, the PS contains a single magnetic null point above the closed field lines. These closed field lines that overlie two (or an even number of) polarity inversion lines are covered by open field lines of the same polarity, without a current sheet, forming the spine of the PS (Rachmeler et al. 2014). Observational studies have suggested that there is a null-point hierarchy: the rolling motions and deflections of prominences are caused by the nearest local null point and the CMEs move in a non-radial direction towards the global null point located at higher altitudes associated to helmet streamers or PS (Panasenco et al. 2013). In order to explain the physical processes involved in the deflection of eruptive phenomena, some numerical studies have been carried out to analyse CME deflections in the presence of PS structures. For example, in a scenario where the heliospheric current sheet and PS are both present, Zuccarello et al. (2012) found a CME that erupts from one of the PS lobes, is initially deflected towards the null point of the PS, and then continues moving towards the heliospheric current sheet. A similar behaviour was found in the simulation performed by Wyper et al. (2021), in which the PS is embedded in a helmet streamer. Recently, Karna et al. (2021) modelled the eruptive filament observed on 2015 April 19, which was embedded in a lobe of the PS and was directed towards the PS null point. Although it is well established both numerically and observationally that FRs inside PSs deflect towards the PS spine (e.g., Török et al. 2011; Zuccarello et al. 2012; Yang et al. 2015; Karna et al. 2021), to date there are no studies that analyse how the trajectory of a FR is affected by variations in the FR–PS configuration.

In this paper, we model cases where only one FR interacts with the PS structure, and we analyse its influence on the FR trajectory at low coronal heights using 2.5 MHD numerical simulations. In Sect. 2, we describe the details of the numerical model and the parameters for the presented cases. In Sect. 3, we present results arising from the several simulations we performed. We find that the FR–PS interactions can be separated into three distinct classes that exhibit differences in the dynamic behaviour of the FR. On one hand, differences in the magnetic field topology lead to different hierarchies of the null points and consequently changes in the dynamical behaviour. On the other hand, we find that the eruption or confinement of the FR strongly depends on the unsigned magnetic flux of the magnetic cage. A discussion and some final remarks are presented in Sect. 4.

## 2. Numerical simulations

To study the interaction between a FR and a PS, we present a scenario where both structures interact in isolation. In this way, we avoid the possible effects of other magnetic structures that could affect the behaviour of the FR, allowing a comprehensive analysis of the influence of the PS on its evolution. We consider the ideal MHD equations in the presence of a gravitational field to solve the 2.5 dimensional model. In CGS units in the Cartesian conservative form we have:

$$\frac{\partial \rho}{\partial t} + \nabla \cdot (\rho \boldsymbol{v}) = 0 \qquad \text{(continuity)} \tag{1}$$

$$\frac{\partial (\rho \boldsymbol{v})}{\partial t} + \nabla \cdot \left( \rho \boldsymbol{v}\boldsymbol{v} - \frac{1}{4\pi}\mathbf{B}\mathbf{B} \right) + \nabla p + \nabla \left( \frac{B^2}{8\pi} \right) = \rho \boldsymbol{g} \qquad \text{(momentum)} \tag{2}$$

$$\frac{\partial E}{\partial t} + \nabla \cdot \left[ \left( E + p + \frac{B^2}{8\pi} \right) \boldsymbol{v} - \frac{1}{4\pi} (\boldsymbol{v} \cdot \boldsymbol{B}) \mathbf{B} \right] = \rho \boldsymbol{g} \boldsymbol{v} \qquad \text{(energy)} \tag{3}$$

$$\frac{\partial \mathbf{B}}{\partial t} + \boldsymbol{\nabla} \cdot (\boldsymbol{v}\mathbf{B} - \mathbf{B}\boldsymbol{v}) = \mathbf{0} \qquad \text{(induction)}, \tag{4}$$

where $\rho$ represents the plasma density, $p$ the thermal pressure, $\boldsymbol{v}$ the velocity, $\mathbf{B}$ the magnetic field, and $\boldsymbol{g}$ the gravity acceleration. $E$ is the total energy (per unit volume) given by

$$E = \rho\epsilon + \frac{1}{2}\rho v^2 + \frac{B^2}{8\pi},$$

where $\epsilon$ is the internal energy and

$$\boldsymbol{j} = \frac{c}{4\pi} \nabla \times \mathbf{B},$$

is the current density, with $c$ being the speed of light.

In addition to the MHD equations, the divergence-free condition of the magnetic field must be fulfilled, that is,

$$\boldsymbol{\nabla} \cdot \mathbf{B} = 0. \tag{5}$$

We assume that the medium is a fully ionised hydrogen plasma, for which the perfect gas law $p = 2\rho k_{\mathrm{B}} T / m_i = (\gamma - 1)\rho\epsilon$ is valid, where $k_{\mathrm{B}}$ is the Boltzmann constant, $T$ the plasma temperature, $m_i$ the proton mass, and $\gamma = 5/3$ the specific heat relation.

Simulations were performed using the FLASH code (Fryxell et al. 2000) in its fourth version, operated under an adaptive refinement mesh with the unsplit staggered mesh (USM) solver, which uses a second-order directionally unsplit scheme with a monotonic upstream-centered scheme for conservation laws (MUSCL)-type reconstruction. We use the local Lax-Friedrichs Riemann solver, which is a diffusive solver providing the necessary dissipation to emulate the magnetic resistivity and use the ideal MHD equations (Sahade et al. 2020). Outflow conditions (zero-gradient) are used at lateral and upper

boundaries, while the line-tied condition is used at the lower boundary, which imposes the condition of null velocity and constant magnetic field for the ghost cells (Robertson & Priest 1987). In the guard cells of the boundary, the magnetic field is linearly extrapolated to preserve the divergence-free configuration. The highest resolution corresponds to $\sim[0.1 \times 0.1]\,\mathrm{Mm}^2$ cells, in a $[-700, 700]\,\mathrm{Mm} \times [0, 700]\,\mathrm{Mm}$ physical domain, where pressure and temperature gradients satisfy the refinement criterion.

### 2.1. FR and PS magnetic model

The modelling of the FR magnetic structure is based on the catastrophe model by Forbes (1990), consisting of an out-of equilibrium magnetic configuration that triggers the FR ejection. The model of the PS is based on the magnetic configuration proposed by Edmondson et al. (2010). However, to better reproduce the decay of the magnetic field with altitude in the solar corona, we replace the constant background magnetic field in the $y$-direction by an exponentially decaying field. The $x$-direction is oriented along the horizontal coordinate, the $y$-direction corresponds to the vertical coordinate, and the $z$-direction is the direction of symmetry. Combining both models, the total magnetic field is given by:

$$
\begin{aligned}
B_x &= B_{x,\mathrm{FR}} + B_{x,\mathrm{PS}},\\
B_y &= B_{y,\mathrm{FR}} + B_{y,\mathrm{PS}},\\
B_z &= B_{z,\mathrm{FR}}.
\end{aligned}
$$

The magnetic field components of the FR are given by the sum of a current wire, an image current wire, and a line dipole:

$$
\begin{aligned}
B_{x,\mathrm{FR}} &= -B_\phi(R_-)\tfrac{(y-h_0)}{R_-} + B_\phi(R_+)\tfrac{(y+h_0)}{R_+}\\
&\quad - MdB_\phi\!\left(r+\tfrac{\Delta}{2}\right)\!\left(r+\tfrac{\Delta}{2}\right)\tfrac{x^2-(y+d)^2}{R_\mathrm{d}^4},\\
B_{y,\mathrm{FR}} &= B_\phi(R_-)\tfrac{x}{R_-} - B_\phi(R_+)\tfrac{x}{R_+}\\
&\quad - MdB_\phi\!\left(r+\tfrac{\Delta}{2}\right)\!\left(r+\tfrac{\Delta}{2}\right)\tfrac{2x(y+d)}{R_\mathrm{d}^4},\\
B_{z,\mathrm{FR}} &= B_z(R_-).
\end{aligned}
\tag{6}
$$

In these expressions, $h_0$ is the initial height of the FR, $M$ is the intensity of the line dipole at depth $d$, $r$ is the current wire radius, $\Delta$ is the thickness of the transition layer between the current wire and the exterior, and $R_\pm = \sqrt{x^2 + (y \pm h_0)^2}$ and $R_\mathrm{d} = \sqrt{x^2 + (y+d)^2}$ are the distances taken from different origins (image and current wire, and dipole, respectively). Also,

$$
B_\phi(R) = \begin{cases}
\frac{2\pi}{c} j_0 R & 0 \le R < r - \frac{\Delta}{2}\\
\frac{2\pi j_0}{cR}\left\{\frac{1}{2}\left(r-\frac{\Delta}{2}\right)^2 - \left(\frac{\Delta}{2}\right)^2 + \right. & \\
\left. \frac{R^2}{2} + \frac{\Delta R}{\pi}\sin\left[\frac{\pi}{\Delta}\left(R-r+\frac{\Delta}{2}\right)\right] + \right. & r-\frac{\Delta}{2} \le R < r+\frac{\Delta}{2}\\
\left.\left(\frac{\Delta}{\pi}\right)^2 \cos\left[\frac{\pi}{\Delta}\left(R-r+\frac{\Delta}{2}\right)\right]\right\} & \\
\frac{2\pi j_0}{cR}\left[r^2 + \left(\frac{\Delta}{2}\right)^2 - 2\left(\frac{\Delta}{\pi}\right)^2\right] & r+\frac{\Delta}{2} \le R
\end{cases}
\tag{7}
$$

$$
j_z(R) = \begin{cases}
j_0 & 0 \le R < r - \frac{\Delta}{2}\\
\frac{j_0}{2}\left\{\cos\left[\frac{\pi}{\Delta}\left(R-r+\frac{\Delta}{2}\right)\right] + 1\right\} & r-\frac{\Delta}{2} \le R < r+\frac{\Delta}{2}\\
0 & r+\frac{\Delta}{2} \le R
\end{cases},
\tag{8}
$$

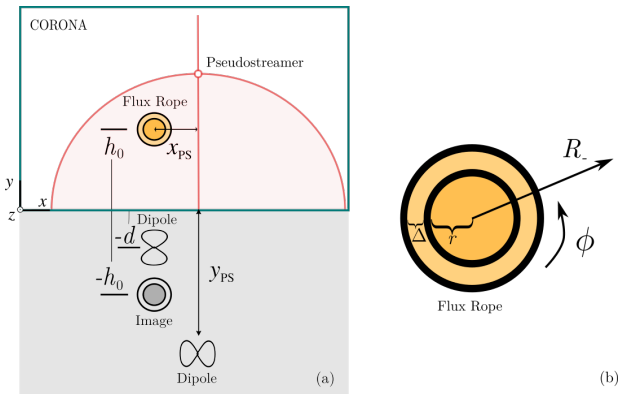


**Fig. 1.** (*a*) FR (orange circle) and PS (red structure) scheme, not to scale. The green frame (*top*) represents the simulated domain and the grey shaded area (*bottom*) contains the magnetic components that are outside of the simulation box. $h_0$ is the FR height and $x_{PS}$ is the distance from the FR to the PS spine (red vertical line), whose height is parametrised by $y_{PS}$. The line dipole and the image current are located at depth $d$ and $h_0$, respectively. (*b*) Internal structure of the FR: $r$ is the radius, $\Delta$ is the thickness of the transition layer, $R_-$ is the radial coordinate from the FR centre, and $\phi$ the poloidal coordinate.

where $j_0$ is a current density. The component $B_z$ of the magnetic field and the current distribution $j_\phi$, are described by

$$
B_z(R) = \tfrac{4\pi j_1}{c}\sqrt{\left(r-\tfrac{\Delta}{2}\right)^2 - R^2},
\tag{9}
$$

$$
j_\phi(R) = j_1 R\left[\sqrt{\left(r-\tfrac{\Delta}{2}\right)^2 - R^2}\right]^{-1},
\tag{10}
$$

where $j_1$ is a current density. These expressions are valid in $0 \le R < r - \frac{\Delta}{2}$ and are null in the rest of the domain.

The magnetic field components of the PS are composed of a line dipole and a potential field:

$$
\begin{aligned}
B_{x,\mathrm{PS}}(x,y) &= \frac{2\sigma B_\mathrm{PS}(x-x_\mathrm{PS})(y-y_\mathrm{PS})}{((x-x_\mathrm{PS})^2 + (y-y_\mathrm{PS})^2)^2}\\
&\quad + B_0\,\sin\left(\frac{x-x_\mathrm{PS}}{H}\right)\exp[-y/H],
\end{aligned}
\tag{11a}
$$

$$
\begin{aligned}
B_{y,\mathrm{PS}}(x,y) &= -\frac{2\sigma B_\mathrm{PS}(x-x_\mathrm{PS})^2}{((x-x_\mathrm{PS})^2 + (y-y_\mathrm{PS})^2)^2}\\
&\quad + \frac{\sigma B_\mathrm{PS}}{(x-x_\mathrm{PS})^2 + (y-y_\mathrm{PS})^2}\\
&\quad + B_0\,\cos\left(\frac{x-x_\mathrm{PS}}{H}\right)\exp[-y/H],
\end{aligned}
\tag{11b}
$$

where $\sigma B_\mathrm{PS}$ is the strength of the magnetic field due to a single line dipole ($\sigma = 2 \times 10^{21}$ is a dimensionless scale factor) positioned at $(x, y) = (x_\mathrm{PS}, y_\mathrm{PS})$, $B_0$ is the strength of the background field at $(x, y) = (x_\mathrm{PS}, 0)$, and $H = 600\,\mathrm{Mm}$ is the height decaying factor.

Figure 1a shows a scheme that indicates the distribution of the magnetic structures, and Fig. 1b shows the internal structure of the FR. The PS model produces a four-flux system, the separation between these regions (red lines) is characterised by a magnetic null point (red circle). Two of the fluxes have a closed topology (red shaded area) and form the PS lobes that are divided by the spine (vertical red line). Outside this region, delimited by the semicircular red line, two open fluxes of equal polarity converge towards the spine and surround the PS structure.

### 2.2. Thermodynamic variables

We simulate the solar atmosphere by adopting a multi-layer structure (Mei et al. 2012). The chromosphere lies between the heights $0 \leq y \leq h_{\rm ch} = 10\,{\rm Mm}$ with constant temperature $T_{\rm ch} = 10\,000\,{\rm K}$. The base of the corona is at a height of $h_{\rm c} = 15\,{\rm Mm}$ and has constant temperature $T_{\rm c} = 10^6\,{\rm K}$. These layers are connected by the transition region, which has a linearly increasing temperature. Thereby, the initial temperature distribution is given by

$$T(y) = \begin{cases} T_{\rm ch} & 0 \leq y < h_{\rm ch} \\ (T_{\rm c} - T_{\rm ch})\left[\frac{y-h_{\rm ch}}{h_{\rm c}-h_{\rm ch}}\right] + T_{\rm ch} & h_{\rm ch} \leq y < h_{\rm c} \\ T_{\rm c} & h_{\rm c} \leq y. \end{cases} \tag{12}$$

The temperature inside the FR ($T_{\rm FR}$) varies according to the following temperature distribution:

$$T(R_-) = \begin{cases} T_{\rm FR} & 0 \leq R < r - \frac{\Delta}{2} \\ (T_{\rm c} - T_{\rm FR})\left[\frac{R_- - (r+\Delta/2)}{\Delta}\right] + T_{\rm FR} & r - \frac{\Delta}{2} \leq R < r + \frac{\Delta}{2} \\ T_{\rm c} & r + \frac{\Delta}{2} \leq R. \end{cases} \tag{13}$$

We consider a current-free atmosphere in hydrostatic equilibrium. Hence, the background pressure $p(y)$ is only a function of height when considering a system with the $y$-axis aligned to the gravity acceleration (i.e., $\boldsymbol{g} = \frac{-GM_\odot}{(y+R_\odot)^2}\boldsymbol{e}_y$, where $G$ is the gravitational constant, $M_\odot$ is the solar mass, $R_\odot$ is the solar radius, and $y = 0$ corresponds to the solar surface). Therefore, the atmospheric pressure is:

$$p(y) = \begin{cases} p_{\rm ch}\exp\left[\frac{\alpha}{T_{\rm ch}}\left(\frac{1}{h_{\rm ch}+R_\odot} - \frac{1}{y+R_\odot}\right)\right] & 0 \leq y < h_{\rm ch} \\ p_{\rm ch}\exp\left[-\int_{h_{\rm ch}}^{y}\frac{\alpha}{T(y')}(R_\odot + y')^{-2}{\rm d}y'\right] & h_{\rm ch} \leq y < h_{\rm c} \\ \frac{k_{\rm B}}{N_A m_i}T_{\rm c}n_{\rm c}\exp\left[-\frac{\alpha}{T_{\rm c}}\left(\frac{1}{h_{\rm c}+R_\odot} - \frac{1}{y+R_\odot}\right)\right] & h_{\rm c} \leq y, \end{cases} \tag{14}$$

where

$$p_{\rm ch}(y) = \frac{k_{\rm B}}{N_A m_i}T_{\rm c}n_{\rm c}\exp\left[\int_{h_{\rm ch}}^{h_{\rm c}}\frac{\alpha}{T(y')}(R_\odot + y')^{-2}{\rm d}y'\right].$$

The number density at height $y = h_{\rm c}$ in the corona is $n_{\rm c} = 3 \times 10^8$, $\alpha = \frac{m_i G M_\odot}{2k_{\rm B}}$, and $N_{\rm A}$ is the Avogadro number. The internal pressure of the FR is obtained by proposing a solution close to the equilibrium:

$$p_{\rm FR}(x,y) = p(y) + \frac{1}{c}\int_R^{r+\frac{\Delta}{2}} B_{\phi(R')}j_{z(R')}{\rm d}R' - \frac{1}{c}\int_R^{r+\frac{\Delta}{2}} B_{z(R')}j_{\phi(R')}{\rm d}R'. \tag{15}$$

The associated plasma densities are obtained from the adopted equation of state, that is:

$$\rho = \frac{m_i p(y)}{2k_{\rm B}T(y)}. \tag{16}$$

### 2.3. Setup

We perform several simulations to analyse the evolution of a FR interacting with different PS configurations. For all cases, we establish a single FR configuration and model the different cases by varying the parameters describing the magnetic structure of the PS. The simulated FR is warm, its temperature is equal to that of the corona ($T_{\rm FR} = 1\,{\rm MK}$), it has an initial height of $h_0 = 30\,{\rm Mm}$, a radius of $r = 2.5\,{\rm Mm}$, and a transition layer thickness of $\Delta = 0.25\,{\rm Mm}$. Its magnetic parameters are $j_0 = 435\,{\rm statA\,cm^{-2}}$, $j_1 = 322\,{\rm statA\,cm^{-2}}$, $M = 1$, and $d = -3.125\,{\rm Mm}$.

**Table 1.** Pseudostreamer parameters and class of interaction between the flux rope and pseudostreamers.

| | $B_0$ [G] | $B_{\rm PS}$ [G] | $x_{\rm PS}$ [Mm] | $y_{\rm PS}$ [Mm] | Class |
|---|---|---|---|---|---|
| PS1-L | 1 | −1.284 | 210 | −360 | $I_e$ |
| PS1-C | 1 | −1.284 | 140 | −360 | $I_e$ |
| PS1-R | 1 | −1.284 | 70 | −360 | $I_e$ |
| PS2-L | 2 | −2.569 | 210 | −360 | $I_{ne}$ |
| PS2-C | 2 | −2.569 | 140 | −360 | $I_{ne}$ |
| PS2-R | 2 | −2.569 | 70 | −360 | $I_e$ |
| PS3-L | 0.5 | −0.203 | 210 | −180 | O |
| PS3-C | 0.5 | −0.203 | 140 | −180 | O |
| PS3-R | 0.5 | −0.203 | 70 | −180 | O |

**Notes.** Parameter $B_0$ determines the magnetic field strength that surrounds the PS. $B_{\rm PS}$ modulates the magnetic field strength inside the PS lobes. The parameters $x_{\rm PS}$ and $y_{\rm PS}$ indicate the position of the dipole that produces the PS lobes. The Class column indicates the initial scenario (I=inner, O=outer) and whether or not the FR erupts (subscripts 'e' and 'ne', respectively).

Table 1 lists the parameters of the selected PSs and the last column provides the resulting interaction class with the FR. To fix the height of the null point ($y_n$) we determine the parameter $B_{\rm PS}$ by zeroing Eq. (11b), that is, $B_{y,{\rm PS}}(x_{\rm PS}, y_n) = 0$. PS1 and PS2 cases correspond to PSs with the null point at a height of ∼280 Mm and lobes of ∼400 Mm in width. PS3 cases have the null point at a height of ∼140 Mm and their lobes are ∼200 Mm in width. Figure 2 shows the magnetic energy density and field lines for each case listed in Table 1. The FR is located to the left of the PS spine. The nomenclature L (left), C (centred), and R (right) indicates the alignment of the FR with respect to the left PS lobe. These cases are representative of a larger sample of performed simulations. They cover the following combination of parameters: background magnetic field $B_0 = \{0.5, 1, 2\}\,{\rm G}$; null point height $y_n = \{140, 280\}\,{\rm Mm}$; lobe width $w \sim \{y_n, 1.5y_n\}$; and FR alignment {R, C, L}. The coupling of the PS and FR magnetic fields alters the PS shape, resulting in a displacement of the PS null point and the appearance of a new null point for all cases. We refer to the PS null point, which is located at a certain height along the spine, as the global null point (GNP). Likewise, we refer to the new null point produced by the addition of the FR as the local null point (LNP).

Two initial scenarios are possible when the PS and FR magnetic field are combined. In one scenario, the LNP is closer to the FR and forms inside the PS structure; the magnetic field lines of the PS lobe that overlay the FR form a confining cage. In the other scenario, the FR field is strong enough to change the PS topology, bending the left lobe field, and the LNP is associated with a new spine-like structure outside the PS; therefore, there is no arcade over the FR forming a magnetic cage. We refer to the interaction resulting from the first scenario as class I (inner; top and middle rows of Fig. 2), and the outcome of the second scenario as a class O (outer) interaction (bottom row of Fig. 2). Class I cases can also be divided according to whether they are eruptive or non-eruptive events (see subscripts 'e' for eruptive,

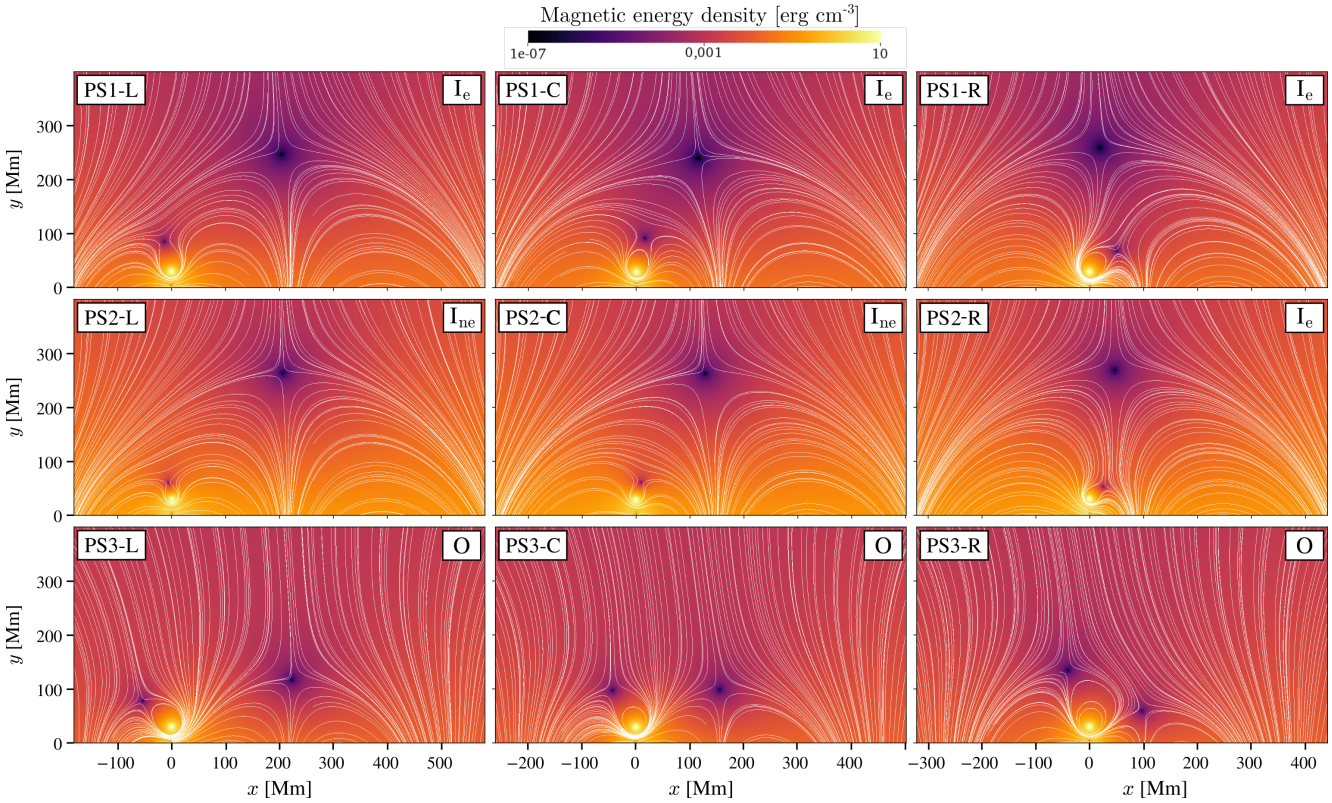


**Fig. 2.** Initial scenarios for the simulations listed in Table 1. The case name and the class of interaction are indicated in boxes to the left and right of each panel, respectively. The colour represents the magnetic energy density, with high density in light yellow and null points shown in dark purple. The magnetic field lines are drawn in white.

and 'ne' for non-eruptive, in Table 1 and Fig. 2). As we show below, the O class has only eruptive events, possibly because the rearrangement of the topology favours the ejection. We focus our attention on the description and analysis of the FR dynamic behaviour and evolution according to the interaction class.

## 3. Results

We present two different analyses: one dynamical and one quantitative. In the first, we analyse and compare how the FR trajectories are influenced by the presence of the LNP and the GNP. For the second, we study the forces that are involved in the dynamics, the unsigned magnetic flux of the magnetic cage, and how the FRs are affected by these factors.

### 3.1. Dynamic behaviour analysis

In this section, we analyse the similarities and differences in the FR deflection depending on the class (I or O) and on whether the event is eruptive or non-eruptive. To facilitate the interpretation of the trajectories, we use a new reference frame defined as $x' = x - x_{\rm GNP}$ centred in the GNP of each PS, and therefore all the spines are centred at 0 $x'$-coordinate. All simulations are analysed until the FR reaches a height of $y = 600$ Mm or $t = 4000$ s, whichever comes first.

#### 3.1.1. Class I

*Eruptive cases.* Cases PS1-L, PS1-C, PS1-R, and PS2-R belong to class I eruptive cases (see top row panels and rightmost panel of the middle row in Fig. 2). All their LNPs are inside the PS. For the cases PS1-L, PS1-C, and PS1-R we consider the same magnetic configuration of the PS but different horizontal distances between the PS spine and the FR (see $x_{\rm PS}$ in Table 1). These relative distances determine different $(x, y)$ positions of the null points. Figure 3 shows the trajectory of the FR for the different eruptive cases. The dashed-line of a given colour represents the FR trajectory, the stars of the same colour indicate the location of its LNP, and the circles indicate the position of its GNP.

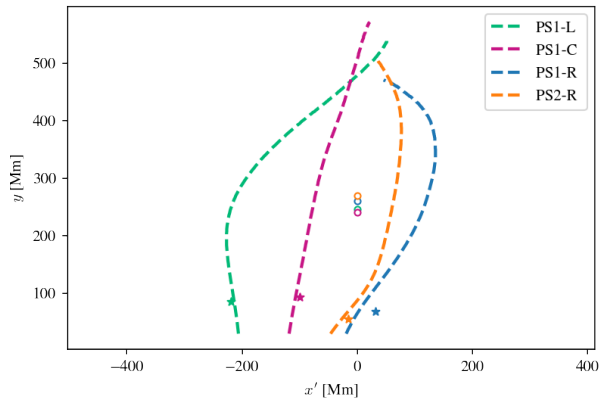


**Fig. 3.** FR trajectories for the class I$_e$ cases. Dashed lines represent the path followed by the FR, stars the LNP location, and circles the GNP position for each case.

There is a common behaviour for class I eruptions. Initially, the FR moves towards the LNP, and therefore the location of the LNP determines the direction of the initial deflection. After

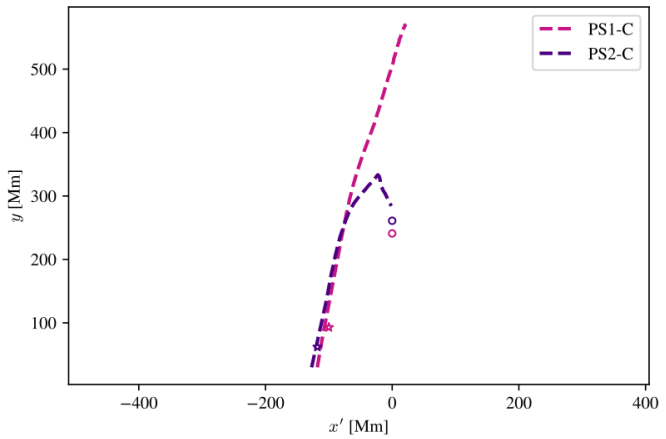


**Fig. 4.** FR trajectories for the cases PS1-C (class $I_e$) and PS2-C (class $I_{ne}$). Dashed lines represent the path, stars the LNP location, and circles the GNP position for each case.

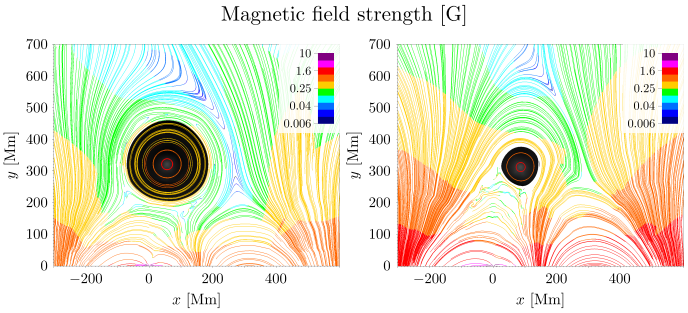


**Fig. 5.** FR position (dark region) and magnetic field line strength of PS1-C (eruptive; *left panel*) and PS2-C (non-eruptive; *right panel*) cases for $t = 1400$ s. The animated evolution of the *right panel* is available online.

that, the LNP is deformed by the displacement of the FR, and the latter continues to rise towards the new direction of low magnetic energy. The FR is guided towards the PS spine, which is located above the GNP. The final directions of all class $I_e$ trajectories eventually converge to a path parallel to the PS spine (which is not always radial). The arrival time and speed on this path will depend on the previous trajectory induced by the LNP. For example, FRs whose initial trajectory is more aligned with the direction of the GNP will be ejected faster (e.g., PS1-C) than those that are deviated by the LNP in an opposite direction to that of the GNP (e.g., PS1-R).

*Non-eruptive cases.* Cases PS2-L and PS2-C are non-eruptive cases of class I (see left and centre panels in the middle row of Fig. 2). PS2 cases have an almost identical morphology to PS1 cases (see top and middle rows of Fig. 2). The difference is that PS2 magnetic fields are twice stronger than PS1 cases. Here we compare PS2-C (non-eruptive) with PS1-C (eruptive); the description is analogous for PS2-L and PS1-L.

Figure 4 shows the trajectory of PS1-C and PS2-C cases for comparison. The initial trajectories are remarkably similar, but at some point the PS2-C case starts a decaying phase and consequently no eruption occurs. The FR continues its descendent motion towards the initial position of the GNP. To understand this behaviour, we display both cases at time $t = 1400$ s in Fig. 5. The dark region highlights the FR location and the colour scale indicates the strength of the magnetic field lines. It can be seen that the volume of the FR for PS1-C is larger than for PS2-C. Studying the environment of the FR, we note that the magnetic cage, which is formed by the set of magnetic field lines from the PS lobe that overlay the FR and confine it, is wider and stronger for PS2-C. The differences between the two cages are most evident in the upper section of the cage, where the higher number of lines constituting the PS2-C cage is clear and their strengths can be compared by the colour levels. In addition, we observe a marked difference in the response of both cages to the rise of the FRs. In case PS1-C, we observe that the cage adapts and follows the shape of the FR, adopting a lock-like shape. In contrast, the PS2-C cage is not sufficiently prone to deformation, and this produces a noticeable imbalance between the fields supporting the FR from below and those confining it above. It is therefore reasonable to infer that this produces a strong magnetic pressure gradient pushing the FR towards the base of the corona, which could trigger the decaying phase. The rigidity of the PS2-C cage may also be the reason for the reduced expansion of the FR, as can be noticed in the animation of the right panel of Fig. 5 (available online). The animation shows the FR rising (until $t = 2000$ s) and its subsequent descent. At this last stage, the FR suffers draining that results in the formation of detached magnetic islands around the FR boundaries. Similar behaviour is observed when comparing PS1-L and PS2-L cases, which share the same path until PS2-L slows its upward motion and finally starts the decaying phase. PS2-L also barely expands and suffers from mass draining.

In summary, the general behaviour of Class I non-eruptive events is characterised by a rising and a decaying phase. During the rising phase, the FR trajectories present the same behaviour as the Class I eruptive events described above. The magnetic cages of non-eruptive cases withstand the upward motion and slow the FR down until the decaying phase begins. During the decaying phase, the FR no longer resists the action of gravity and is guided by the ambient magnetic field lines towards the chromosphere. In addition, non-eruptive FRs expand weakly under the pressure of the ambient magnetic field and become smaller as their outer parts split into detached magnetic islands, sometimes completely destroying the identity of the FR.

### 3.1.2. Class O

The triad PS3-L, PS3-C, and PS3-R belongs to the class O events. These have a common PS structure, but the FR horizontal position is different for each of them. Because these cases are topologically different from the class I cases (see bottom row of Fig. 2), the FR trajectories are not affected in the same way by the null points. They have their own spine-like structure whose base is located at the LNP. Figure 6 shows the trajectories for the PS3 cases. It can be seen that PS3-L and PS3-C are barely affected by the GNP, heading initially towards their LNP and then continuing upwards into their own spine zone, guided by the open magnetic field lines of this spine. However, the PS3-R case, whose initial position is almost equidistant from the two null points, travels between them before reaching the spine of the LNP.

In summary, the FR trajectories for class O are initially headed towards their LNP and then continue upwards towards their own spine-like zone. The events are not influenced by the GNP except when the FR is relatively close to it. Moreover, simulations in this scenario always erupt, seemingly because the LNP is directly connected to the open field lines and there is no magnetic cage above the FR.

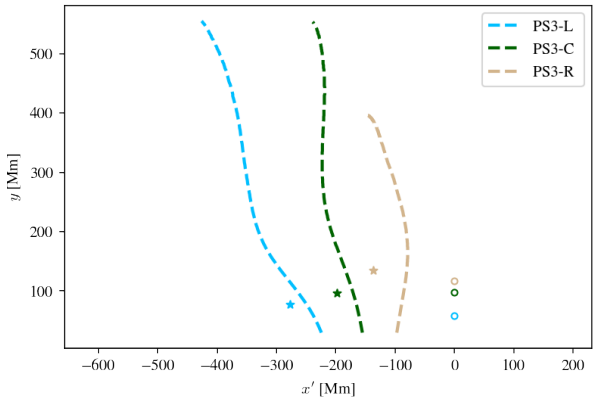


**Fig. 6.** FR trajectories for the class O cases: PS3-R, PS3-C and PS3-L. Dashed lines represent the path, stars the LNP location, and circles the GNP position for each case.

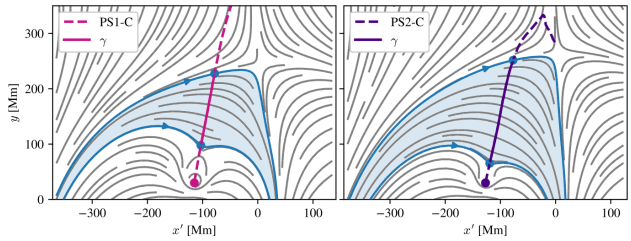


**Fig. 7.** Magnetic field lines for events PS1-C (*left*) and PS2-C (*right*). The shaded light blue areas represent the magnetic cage above the FR, and the magenta and indigo dots indicate the initial position for PS1-C and PS2-C, respectively. The solid line represents the internal trajectory of the FR through which the flux of the magnetic cage is quantified.

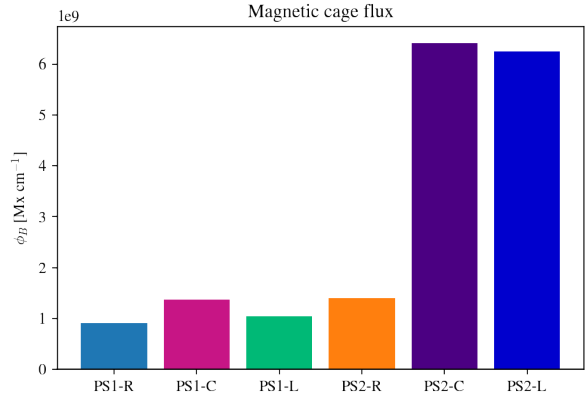


**Fig. 8.** Total unsigned magnetic flux per unit length of the magnetic cage for PS1 and PS2 cases.

### 3.2. Quantitative analysis

In this section, we focus on the magnetic cage and its effect on FR evolution. More precisely, we define a magnetic cage as the structure formed by all the field lines enclosing the FR and whose two ends are attached to the base of the corona (height $y = 0$). As suggested previously by Fig. 5, the magnetic cage of the non-eruptive events is larger and more intense than that of the eruptive cases. Figure 7 shows the magnetic cages for the PS1-C and PS2-C cases shaded in light blue. Inspired by the results of Li et al. (2020, 2021, 2022), we also determine the total unsigned magnetic flux to quantify the strength of the magnetic cages. Taking advantage of the symmetry considered in the

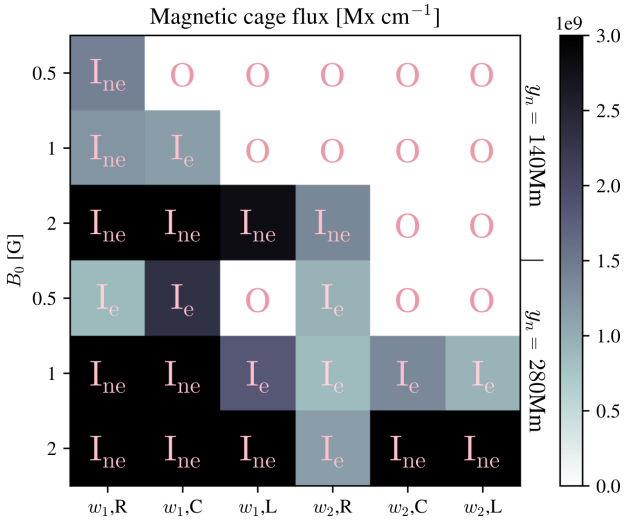


**Fig. 9.** Parameter map for the simulation set. The colour bar represents the magnetic cage flux strength. The $B_0$ parameter is the background magnetic field related to the PS, $w_1$ and $w_2$ refer to the PS lobe widths, R-C-L are the FR alignments, and $y_n$ is the PS null point height. For each box the dynamical behaviour is indicated.

$z$-direction, we calculate the initial magnetic flux per unit length $\phi_B$ through a path outlined by the FR trajectory as follows:

$$\phi_B = \frac{1}{L_z}\int_A |\mathbf{B}\cdot \mathrm{d}A| = \int_\gamma |B_\perp|\,\mathrm{d}S, \tag{17}$$

where $B_\perp$ is the magnetic field transverse to a curve $\gamma$ defined by the FR path (denoted by the solid coloured lines in Fig. 7). Figure 8 shows the total unsigned magnetic flux of each magnetic cage for all PS1 and PS2 cases (PS3 cases do not produce magnetic cages). We note that the magnetic flux values for the non-eruptive cases (PS2-L and PS2-C) are remarkably large in comparison to the eruptive cases.

To understand how the dynamical behaviour is affected by the simulation parameters, we include in Fig. 9 the magnetic cage flux (represented by the colours of the colour bar) for the whole simulation set as a function of $B_0$ ($y$-axis) and width alignment ($x$-axis). The widths ($w$) are $w_1 \sim y_n$ and $w_2 \sim 1.5y_n$, with $y_n$ being the height of the null point, and the alignment R-C-L as described in Sect. 2.3. We also separate the cases according to $y_n$ (top and bottom parts of the plot) with the values denoted on the right. For each case, we indicate its classification as defined in the previous section. We again notice the correlation between larger magnetic cage fluxes and non-eruptive cases. In addition, these cases are more closely related to stronger $B_0$ magnetic fields and narrower PSs ($w_1$). This is expected as these parameters influence the magnetic flux of the PS lobe. However, the magnetic cage flux will also depend on the position and parameters of the FR, that is, on how many lobe lines actually belong to the cage.

We also analyse the evolution of the FR variables for PS1 and PS2 cases to understand how they are affected by the magnetic cage. PS3 cases are not included because they do not present a magnetic cage and, moreover, they follow the trends of class $\mathrm{I_e}$. First, we analyse the evolution of FR velocity and total force in the $y$-direction. Figure 10 shows the vertical velocity curves ($v_y$) up to $t = 1000$ s. The initial force for non-eruptive cases (PS2-L and PS2-C) is stronger and pushes the FRs towards the LNP with notably higher speeds, which is likely due to the closer proximity to the LNP. However, after reaching the maximum value,

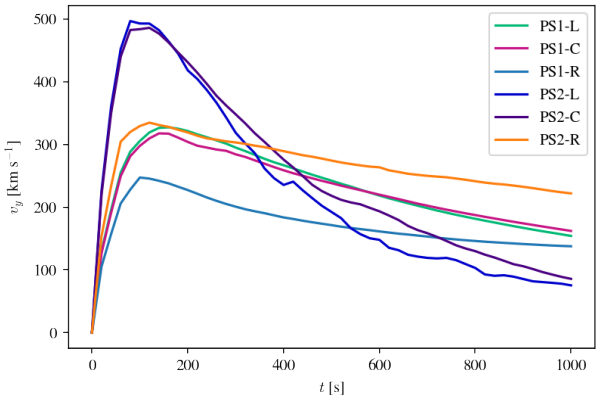


**Fig. 10.** Vertical velocity $v_y$ as a function of time for PS1 and PS2 cases.

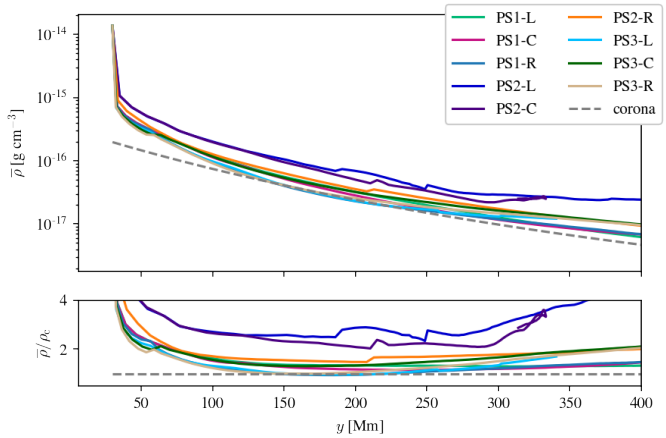


**Fig. 11.** Average plasma density of the FR as a function of height. The dashed grey line represents the plasma density of the corona. The *lower panel* shows the corresponding ratio between the plasma density for each case and the coronal plasma density $\rho_c$.

the $v_y$ of $I_{ne}$ events decreases more and steeper than the $v_y$ of $I_e$ events. Eventually, $v_y$ becomes negative and the decaying phase of the FR starts. From the separate analysis of the force components (magnetic pressure and tension, gas pressure, and gravity, not shown here), we find that the magnetic pressure gradient is the main factor responsible for the abrupt deceleration and the descent of the FR, after which gravity is the dominant decelerating force. This result is in agreement with the qualitative analysis presented in the previous section, in which we note that the concentration of field lines over the FR (see Fig. 5) seems to be responsible for exerting this magnetic pressure force. Gravity becomes the leading force once the FR is 'channelled' by the lobe magnetic field lines (decaying phase).

From the analysis of the FR variables, we note the major differences (between $I_e$ and $I_{ne}$ cases) in the evolution of the hydrodynamic variables. As we also mentioned in the previous section, the volume of the non-eruptive FRs remains small, contained by the strong magnetic cage surrounding them. Thus, the plasma density and gas pressure for non-eruptive FRs is higher than for the eruptive FRs, which manage to expand. Figure 11 shows the evolution of the FR average plasma density as a function of height, together with the coronal plasma density $\rho_c$ (dashed grey line). Initially, all FRs are overdense and their average density quickly decreases because they are out of external equilibrium. Afterwards, the density continues to decrease as the FRs expand, following the drop in ambient pressure with altitude. However, as the non-eruptive FRs (PS2-L and PS2-C) almost completely stop expanding, their densities tend asymptotically to a certain value. In the bottom panel of Fig. 11, we present the ratio between the FR and coronal density, which highlights the balance between the weight and the buoyant force. We note an important difference between eruptive and non-eruptive cases: while the former manage to reach densities similar to that of the corona, the non-eruptive ones remain at more than twice the coronal density due to the lack of expansion. Consequently, the buoyant force of these last cases is not strong enough to overcome the gravitational field and the action of the magnetic cage, and so an eruption is not produced.

## 4. Discussion and conclusions

In this work, we analyse the dynamic behaviour of a FR located near an isolated PS. The magnetic configuration produces the emergence of two magnetic null points associated with both structures: a LNP formed by the cancellation of the FR and PS magnetic fields, and a GNP related to the PS itself. We note that the LNP is determinant for the early evolution of the FR. All simulated cases show an initial deflection due to the attraction towards this point of low magnetic energy. The subsequent evolution depends on whether the FR is enclosed by the PS lobes (class I events) or not (class O), showing that the hierarchy of the null points depends on the topology. In class O, the LNP is associated to an intrinsic spine-like configuration and the FR is guided by its open magnetic field lines instead of travelling towards the PS spine. For class I events, a second deflection can take place by the influence of the GNP, directing the FR to the PS spine. In this scenario, it is possible that the eruption fails. We determine that the magnetic cage – formed by the magnetic field lines from the PS lobe that encloses the FR – plays a crucial role in curbing the eruption.

The non-eruptive cases, which initially reach higher velocities, are quickly decelerated by the magnetic cage. The cage field lines are compressed instead of adjusting to the rise of the FR, producing high magnetic pressure gradients that force the FR back to the surface. Also, we note for these cases that the expansion of the FR is inhibited by the magnetic cage, keeping it overdense and less buoyant, which helps to prevent the eruption. Thus, we quantified the total unsigned magnetic fluxes of the cages, obtaining that in the non-eruptive cases the average value is almost six times higher than in the eruptive cases. This magnitude can be interpreted as a measure of the magnetic cage resistance. We also show that cases with stronger magnetic field $B_0$ and narrower PS lobe width $w$ are prone to be non-eruptive.

We show that the combination of a FR with a PS magnetic structure is topologically complex. Although the relative position between the FR and PS centre plays an essential role in predicting the non-radial motions of the FR trajectory, the magnetic flux contained in the magnetic cage seems to be the key parameter in determining whether or not an eruption can occur, in agreement with previous studies. Hence, we consider it to be of utmost importance to attain improved magnetic field measurements such as those that will be provided by missions like Solar Orbiter, PUNCH (Polarimeter to UNify the Corona and Heliosphere), and Aditya, among others, in order to analyse more observational events that can be compared with our results and to refine numerical models that contribute to space weather forecasts.

*Acknowledgements.* We would like to thank the anonymous reviewer for very useful comments that helped us to improve this work. AS is doctoral fellow

of CONICET. MC, GK, HC and AC are members of the Carrera del Investigador Científico (CONICET). AS and MC acknowledge support from ANPCyT under grant number PICT No. 2016-2480. AS, MC, MVS and AC also acknowledge support by SECYT-UNC grant number PC No. 33620180101147CB. AS, MC, MVS and AC acknowledge support from PIP under grant number No. 11220200103150CO. MVS acknowledges support from the European Research Council (ERC) under the European Union's Horizon 2020 research and innovation programme (grant agreement No 724326). HC appreciates support from grants MSTCAME8181TC (UTN) and PIP 11220200102710CO (CONICET). Also, we thank the Centro de Cómputo de Alto Desempeño (UNC), where the simulations were carried out.

## References

Amari, T., Canou, A., Aly, J.-J., Delyon, F., & Alauzet, F. 2018, Nature, 554, 211
Baumgartner, C., Thalmann, J. K., & Veronig, A. M. 2018, ApJ, 853, 105
Bi, Y., Jiang, Y., Yang, J., et al. 2013, ApJ, 773, 162
Cécere, M., Sieyra, M. V., Cremades, H., et al. 2020, AdSpR, 65, 1654
Chen, H., Ma, S., & Zhang, J. 2013, ApJ, 778, 70
Cremades, H., Bothmer, V., & Tripathi, D. 2006, AdSpR, 38, 461
Edmondson, J. K., Antiochos, S. K., DeVore, C. R., & Zurbuchen, T. H. 2010, ApJ, 718, 72
Filippov, B. 2021, PASA, 38, e018
Filippov, B. P. 2019, Phys. Uspekhi, 62, 847
Forbes, T. G. 1990, J. Geophys. Res., 95, 11919
Fryxell, B., Olson, K., Ricker, P., et al. 2000, ApJS, 131, 273
Gopalswamy, N., Mäkelä, P., Xie, H., Akiyama, S., & Yashiro, S. 2009, J. Geophys. Res. (Space Phys.), 114, A00A22
Green, L. M., Török, T., Vršnak, B., Manchester, W., & Veronig, A. 2018, Space Sci. Rev., 214, 46
Gronkiewicz, D., Mrozek, T., Kołomański, S., & Chruślińska, M. 2016, in Solar and Stellar Flares and their Effects on Planets, eds. A. G. Kosovichev, S. L. Hawley, & P. Heinzel, 320, 221
Jiang, C., Feng, X., & Hu, Q. 2018, ApJ, 866, 96
Jing, J., Liu, C., Lee, J., et al. 2018, ApJ, 864, 138
Karna, N., Savcheva, A., Gibson, S., et al. 2021, ApJ, 913, 47
Kay, C., Opher, M., & Evans, R. M. 2013, ApJ, 775, 5
Kay, C., Opher, M., & Evans, R. M. 2015, ApJ, 805, 168
Li, T., Hou, Y., Yang, S., et al. 2020, ApJ, 900, 128
Li, T., Chen, A., Hou, Y., et al. 2021, ApJ, 917, L29
Li, T., Sun, X., Hou, Y., et al. 2022, ApJ, 926, L14
Liewer, P., Panasenco, O., Vourlidas, A., & Colaninno, R. 2015, Sol. Phys., 290, 3343
Mei, Z., Shen, C., Wu, N., et al. 2012, MNRAS, 425, 2824
Möstl, C., Rollett, T., Frahm, R. A., et al. 2015, Nat. Commun., 6, 7135
Panasenco, O., Martin, S. F., Velli, M., & Vourlidas, A. 2013, Sol. Phys., 287, 391
Rachmeler, L. A., Platten, S. J., Bethge, C., Seaton, D. B., & Yeates, A. R. 2014, ApJ, 787, L3
Robertson, J. A., & Priest, E. R. 1987, Sol. Phys., 114, 311
Sahade, A., Cécere, M., & Krause, G. 2020, ApJ, 896, 53
Sahade, A., Cécere, M., Costa, A., & Cremades, H. 2021, A&A, 652, A111
Shen, C., Wang, Y., Gui, B., Ye, P., & Wang, S. 2011, Sol. Phys., 269, 389
Sieyra, M. V., Cécere, M., Cremades, H., et al. 2020, Sol. Phys., 295, 126
Török, T., & Kliem, B. 2005, ApJ, 630, L97
Török, T., Panasenco, O., Titov, V. S., et al. 2011, ApJ, 739, L63
van Driel-Gesztelyi, L., & Green, L. M. 2015, Liv. Rev. Sol. Phys., 12, 1
Wang, Y. M. 2015, ApJ, 803, L12
Wang, Y., & Zhang, J. 2007, ApJ, 665, 1428
Wang, R., Liu, Y. D., Dai, X., et al. 2015, ApJ, 814, 80
Wang, J., Hoeksema, J. T., & Liu, S. 2020, J. Geophys. Res. (Space Phys.), 125
Wyper, P. F., Antiochos, S. K., DeVore, C. R., et al. 2021, ApJ, 909, 54
Yang, J., Jiang, Y., Xu, Z., Bi, Y., & Hong, J. 2015, ApJ, 803, 68
Yang, J., Dai, J., Chen, H., Li, H., & Jiang, Y. 2018, ApJ, 862, 86
Zhang, J., Dere, K. P., Howard, R. A., Kundu, M. R., & White, S. M. 2001, ApJ, 559, 452
Zuccarello, F. P., Bemporad, A., Jacobs, C., et al. 2012, ApJ, 744, 66